PHYSICAL REVIEW B VOLUME 15, NUMBER 4 15 FEBRUARY 1977

Magnetoacoustic resonance attenuation in Ga-doped Ge

H. Tokumoto and T. Ishiguro
Electrotechnical Laboratory, Mukodai, Tanashi, Tokyo 188, Japan
(Received 7 September 1976)

The magnetoacoustic resonance attenuation (MARA), which is observed in Ga-doped Ge under strong magnetic field at low temperatures, is studied in detail by varying the acoustic frequency, the temperature, the magnetic field direction, the acceptor concentration, the acoustic power, the acoustic mode, the propagation direction, and the uniaxial stress. The experimental results are explained semiquantitatively in terms of the acceptor-hole-lattice interaction in the effective-mass approximation by taking account of the presence of the distributed local splittings and the quadratic Zeeman effect in addition to the linear Zeeman effect. Consequently, the Zeeman-splitting parameters of the ground state in Ga-doped Ge are obtained. The g values are $g_{1/2}' = -0.14 \pm 0.07$ and $g_{3/2}' = 0.02 \pm 0.03$ for $\vec{H} \parallel [001]$. The discrepancy between the present results and the results derived from the magneto-optical absorption by Soepangkat and Fisher is resolved by proposing a new assignment of their magneto-optical spectra. The coefficients of the quadratic Zeeman effect are $q_2 = (0.5 \pm 0.2) \times 10^{-4}$ K/kG^2 and $q_3 = -(0.6 \pm 0.2) \times 10^{-5}$ K/kG^2. The present g values, which are very small compared with the effective-mass calculations, seem to be consistent with the measured magnetothermal conductivity and the present status of the ESR study. From the line shape of the MARA, we evaluated the initial splittings of the acceptor ground-state. When we assume that their distribution is represented by the Gaussian form, the average splitting Δ_0 and the variance σ are obtained as -0.02 ± 0.006 K and 0.03–0.05 K, respectively.

I. INTRODUCTION

The electronic states of shallow impurities in semiconductors are represented by the hydrogenic states. When the average distance among the impurity atoms is larger than their effective Bohr radius, we can neglect the interaction among them in the first-order approximation. The localized shallow impurities interact with acoustic phonons strongly. This has been seen as a remarkable increase at low temperatures in either the thermal resistance[1-10] or the ultrasonic attenuation.[11-19]

The thermal resistance and the ultrasonic attenuation in lightly doped n-type Ge and n-type Si at low temperatures have been understood rather well: They are explained by the interaction of the acoustic phonons with the localized donors whose electronic states are represented by the effective-mass approximation.[1-4, 11-16] However, the problem on the interaction with the localized acceptors has remained unsettled.

The strong increase of the ultrasonic attenuation in p-Si as decreasing the temperature below 20 K was first ascribed to the effect of free holes.[17] Pomerantz,[18] however, pointed out that the holes are frozen into the acceptor ground state in adopted experimental conditions. Suzuki and Mikoshiba[19] (SM) proposed a model to explain the ultrasonic attenuation in lightly doped p-Si at low temperatures: (a) They calculated the coupling of the ultrasonic waves with the acceptors in the regime of the effective-mass approximation.[20,21] (b) They assumed the presence of the randomly distributed internal stresses, which split the fourfold-degenerate acceptor ground state into two Kramers doublets.[22] The observed ultrasonic attenuations in lightly doped p-Si at low temperatures as functions of the temperature,[17,23,24] the uniaxial stress,[25] the magnetic field,[24,26] the dislocation density,[24] and the acceptor concentration[24] are consistent with the SM model. This model is also consistent with the thermal conductivity[27] and the heat-pulse propagation[28] in p-Si. In lightly doped p-Ge, this model is useful to explain the temperature dependence of the thermal conductivity[27] and the heat-pulse propagation.[28] Challis and Halbo,[29] however, have reported that this model is not adequate for the analysis of the magnetic field dependence of the thermal conductivity in p-Ge. They proposed that the existence of low-lying states due to the dynamic Jahn-Teller effect[30] should be taken into account.

In order to clarify the anomalous magnetothermal conductivity in p-Ge,[29,31] we measured the magnetic field dependence of the ultrasonic attenuation in Ga-doped Ge. Then, we found a resonance attenuation under strong magnetic fields,[32] which was observed in neither B-doped Si nor Zn-doped GaP. The resonance attenuation seemed to be explained by an extension of the SM model; we had taken the quadratic Zeeman effect of the acceptor ground state into account,[32] in addition, to the linear Zeeman effect whose parameters are reported by Soepangkat and Fisher[33] (SF).

We have extended the experiment of the magnetoacoustic-resonance attenuation (MARA) by

varying the acoustic frequency, the temperature, the magnetic field direction, the acceptor concentration, the acoustic power, and the acoustic mode, and also by applying the uniaxial stress. It turned out, then, that the Zeeman-splitting parameters adopted previously[32] were not adequate to explain all of the observed results consistently. We found that the g values of the acceptor ground state, which are derived by SF, could not be consistent with our experimental results at all. In this paper, we propose new g values which are useful to explain our observations and also are consistent with the experimental results by SF[33]: An alternative assignment of the observed magnetooptical spectra is consistent with the new g values.

The purpose of this paper is to show the detailed description on the MARA as functions of the temperature and so on, and to present a successful interpretation of them. We will show that the experimental results are explained by the extension of the SM model by taking account of the quadratic Zeeman effect. From the comparison of the resonance fields with the calculated energy-level shifts of the acceptor-ground-state quartet, we have determined the g values and some coefficients of the quadratic Zeeman effect. The consistency of these values with other experimental results, the magneto-optical spectra[33] and the magneto-thermal conductivity,[29,31] are discussed.

II. EXPERIMENTAL PROCEDURE

Five different samples of Ga-doped Ge were used. All samples were in the shape of rectangular parallelepipeds. The sample characteristics are listed in Table I. The acceptor concentrations N were estimated by the resistivities.[34] Since $R \geq 6a^*$ is satisfied in our samples [$R = (3/4\pi N)^{1/3}$, a^* is the effective Bohr radius], we may regard the acceptors isolated in the first-order approximation.

TABLE I. Characteristics of the samples.

Sample No.	Resistivity (Ω cm)	EPD[a] (cm^{-2})	N[b] (10^{15} cm^{-3})	$\vec{q}$[c]
1	1.1–1.2	~700	3.5±0.7	[001]
2	1.1–1.2	~700	3.5±0.7	[110]
3	1.1–1.2	~700	3.5±0.7	[110]
4	0.50–0.55	~900	7.0±0.6	[001]
5	0.19–0.20	~400	25±5	[001]

[a] EPD denotes the etch pit density.

[b] N is the Ga concentration estimated by the resistivity after Ref. 34.

[c] $\vec{q}$ denotes the propagation direction of the ultrasonic waves.

The crystals were oriented by x ray and cut to the orientations shown in Table I. The end faces normal to the propagation direction of the ultrasonic waves were lapped and polished to be parallel within 10–20 sec of arc. The end faces perpendicular to the uniaxial stress direction were also lapped and polished to within parallelism of 1 min of arc. The samples were set to the sample holder with great care in order to avoid giving stresses except for the case measuring the stress dependence.

The ultrasonic attenuation was measured by the standard pulse-echo technique. The sputtered ZnO piezoelectric film transducer was used in order to avoid giving stresses to the sample. The ultrasonic attenuation was measured as a function of the magnetic field with a logarithmic converter by selecting one of the ultrasonic echos with a boxcar integrator. In the present measurement, the pulse repetition rate of 50–100 Hz and the pulse duration of 0.5–1.0 μsec were used. The overall nonlinearity of the apparatus used was less than 5%.

Static magnetic fields up to 120 kG were applied to the sample by using a superconducting magnet. The magnetic field strength was monitored by the calibrated magnetoresistance of a copper wire. Uniaxial stress was applied to the sample by using the stress apparatus designed to minimize nonuniformity of the stress.

III. THEORY

A. Interaction of the ultrasonic waves with the acceptor holes (Ref. 19)

The coupling of the acoustic phonons with the acceptor holes and the splitting of the acceptor-ground-state quartet by an external stress are dealt with a strain Hamiltonian[21]

$$H^a_{\text{strain}} = \tfrac{2}{3}D^a_u[(J_x^2 - \tfrac{1}{3}J^2)e_{xx} + \text{c.p.}] + \tfrac{1}{3}D^a_{u'}[(J_xJ_y + J_yJ_x)e_{xy} + \text{c.p.}], \quad (3.1)$$

where J_α is the α component of the angular momentum operator for $J = \frac{3}{2}$, $e_{\alpha\beta}$ is the conventional strain component, c.p. denotes the cyclic permutation with respect to the indices x, y, and z, and D^a_u and $D^a_{u'}$ are the deformation-potential constants for the acceptor ground state.

Using the strain Hamiltonian (3.1) and the acceptor-ground-state wave functions,[21] we can derive the ultrasonic-attenuation formula. Following Kwok's method,[14] the attenuation coefficient is given by[19]

$$\alpha = \frac{\omega_{\vec{q}t}}{\rho v_t^3}\frac{\hbar\omega_{\vec{q}t}}{kT}\sum_{n,n'} N_n(\tfrac{2}{3}D^a_{u'})^2 |C^{nn'}_{\vec{q}t}|^2 \times \frac{\Gamma_n + \Gamma_{n'}}{(\hbar\omega_{\vec{q}t} - E_{n'n})^2 + (\Gamma_n + \Gamma_{n'})^2}, \quad (3.2)$$

where the states corresponding to $M_J = \frac{3}{2}, \frac{1}{2}, -\frac{1}{2}, -\frac{3}{2}$ are labeled by $n = 1$, 2, 3, and 4, respectively. $\omega_{\vec{q}t}$ is an angular frequency for the phonons of the wave vector $\vec{q}$ and in branch t ($t = 1$, 2, and 3 refer to the longitudinal, the fast-transverse and the slow-transverse branches, respectively). v_t is the sound velocity in branch t, and ρ is the crystal density. The $C_{\vec{q}t}^{nn'}$ are referred to coupling parameters, whose explicit expressions are given by SM[27] and Fjeldly *et al.*[28] In Eq. (3.2),

$$E_{n'n} = E_{n'} - E_n , \tag{3.3}$$

N_n and Γ_n are the number of holes per unit volume and the level width in the nth level. These expressions are derived under the following assumptions: The crystal is elastically isotropic. The small amount of the d-like parts in the acceptor-ground-state wave functions is neglected.

In order to perform the calculation in an analytically tractable way, SM have made the following assumptions[19]: (i) The ground-state quartet is split by the randomly distributed local strains by an amount Δ. (ii) These internal strains are represented by the normal stresses in the [111] and its equivalent directions. (iii) The distribution of Δ is represented by the Gaussian or Lorentzian form. We take the Gaussian form here as

$$g(\Delta) = (2\pi)^{-1/2}\sigma^{-1} \exp[-(\Delta - \Delta_0)^2/2\sigma^2] , \tag{3.4}$$

where Δ_0 is the average value of Δ and σ the variance. (iv) The level width Γ_n is determined by the direct (one-phonon) and Raman (two-phonon)[35] processes as

$$\Gamma_n = \Gamma_n^d + \Gamma_{Rn} . \tag{3.5}$$

The Γ_{Rn} is almost independent of n and the explicit expression is given in Ref. 19.

The measured attenuation coefficient α is obtained by integrating $\alpha(\Delta)$ which is a function of Δ;

$$\alpha = \int_{-\infty}^{\infty} \alpha(\Delta) g(\Delta)\, d\Delta . \tag{3.6}$$

The expression of $\alpha(\Delta)$ in the absence of the magnetic field is given in Ref. 19. When both the magnetic field and the uniaxial stress are applied in the [001] direction, the expressions of $E_{n'n}$, $C_{\vec{q}t}^{nn'}$, Γ_n^d, and N_n in Eq. (3.2) for the transverse waves ($t = 2$) propagating along either the [001] or the [110] directions are obtained as shown in Appendix A. When the magnetic field is applied in the [111] direction, the similar expressions for the above parameters are obtained.[36]

B. Zeeman splitting of the acceptor ground state

Several calculations have been reported on the Zeeman effect of the shallow acceptors in germanium. Some of these[21,37,38] have utilized either the effective-mass wave functions[39] or the effective-mass formalism and have obtained the explicit g values as listed in Table II. For studying the Zeeman effect of the acceptor state in germanium and silicon, Bhattacharjee and Rodriguez[40] (BR) have adopted a group theoretical treatment. Then BR have derived the energies of the Zeeman sublevels for $\vec{H} \| [001]$ as[40]

$$E_{M_J} = \mu_B (g_1' M_J + g_2' M_J^3) H + [q_1 + (q_2 + q_3) M_J^2] H^2 , \tag{3.7}$$

where $M_J = \frac{3}{2}$, $\frac{1}{2}$, $-\frac{1}{2}$, and $-\frac{3}{2}$. In the case of $\vec{H} \| [111]$, the energies are given by[40]

$$E_{\pm 3/2} = \pm\mu_B [(\tfrac{3}{2} g_1' + \tfrac{23}{8} g_2')^2 + \tfrac{1}{2} g_2'^2]^{1/2} H + (q_1 + \tfrac{9}{4} q_2 + \tfrac{5}{4} q_3) H^2 , \tag{3.8}$$

$$E_{\pm 1/2} = \pm\mu_B (\tfrac{1}{2} g_1' + \tfrac{13}{8} g_2') H + (q_1 + \tfrac{1}{4} q_2 + \tfrac{5}{4} q_3) H^2 . \tag{3.9}$$

IV. EXPERIMENTAL RESULTS

A. Temperature dependence of the attenuation in the absence of the magnetic field

Prior to the description of the MARA, we show the temperature dependence of the ultrasonic attenuation in the absence of the magnetic field. In Fig. 1 are shown the temperature dependences of

TABLE II. g values of the acceptor ground state in Ge for $\vec{H} \| [001]$. The second entry for SP is discussed in the text.

	g_1'	g_2'	$g_{1/2}'$	$g_{3/2}'$
Bir *et al.*[a]	5.66	−0.26	5.60	5.10
SOH[b]	−1.44	0.56	−1.30	−0.19
LCW[c]	−1.13	0.63	−0.97	0.29
SP[d]	−1.73 ± 0.11	0.78 ± 0.07	−1.53 ± 0.09	0.03 ± 0.04
	−0.26 ± 0.11	0.12 ± 0.07	−0.22 ± 0.09	0.03 ± 0.04
Present	−0.16 ± 0.08	0.08 ± 0.04	−0.14 ± 0.07	0.02 ± 0.03

[a] See Ref. 37.
[b] See Ref. 21.
[c] See Ref. 38.
[d] See Ref. 33. These g values are for B-doped Ge.

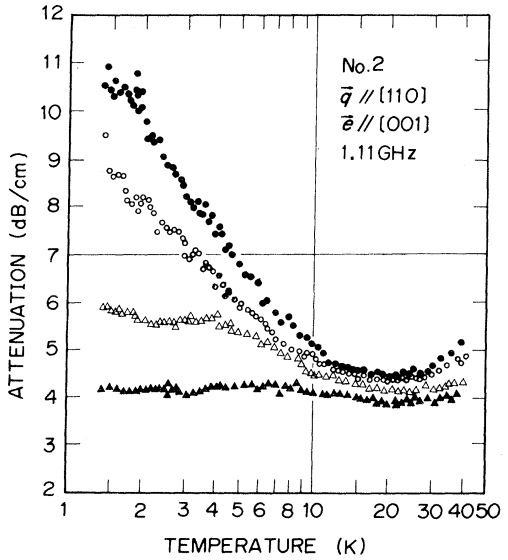

FIG. 1. Temperature dependences of the attenuation of the 1.11-GHz fast transverse waves propagating along the [110] direction in sample No. 2. Closed and open circles denote the attenuations at the acoustic-power levels of 0.01 and 0.06 mW/cm^2, respectively. Open and closed triangles denote those at 0.6 and 6 mW/cm^2, respectively.

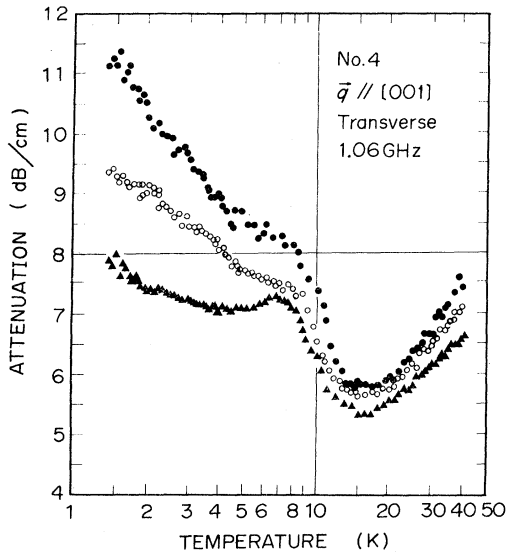

FIG. 2. Temperature dependences of the attenuation of the 1.06-GHz transverse waves propagating along the [001] direction in sample No. 4. Closed circles, open circles, and triangles denote the attenuations at the acoustic-power levels of 0.03, 0.1, and 1 mW/cm^2, respectively.

the attenuation of the 1.11-GHz fast transverse waves in sample No. 2 at four acoustic power levels. The attenuation increases with decreasing the temperature below 15 K except for the case of 6 mW/cm^2, which changes little with the temperature. The residual attenuations of ~4 dB/cm are caused by the following facts; the scattering by defects, the lack of the parallelism of the sample faces, and the interference of the ultrasonic waves reflected at two faces of a ZnO film. The attenuations at low temperatures decrease with increasing the acoustic power; the saturation effect[41] is observed. The temperature dependences of the attenuations of the transverse and the longitudinal waves in sample No. 1 are similar to the case shown in Fig. 1.

The results for the 1.06-GHz transverse waves in sample No. 4 are shown in Fig. 2 at three acoustic power levels. The feature of the temperature dependence is similar to the above cases except for an attenuation increment near 7 K. This increment becomes clear with increasing the acoustic power. The temperature dependence of the attenuation in sample No. 5 is similar to the case in No. 4 except for an amount of the attenuation.

B. Magnetoacoustic resonance attenuation

We measured the magnetic field dependence of the ultrasonic attenuation in five samples (Table I). Magnetic fields up to 120 kG were applied in the $(1\bar{1}0)$ plane. The attenuation was measured in the temperature range 1.3–4.2 K at a fixed acoustic power level.

The effect of the magnetic field on the attenuation in sample No. 1 is shown in Fig. 3. When the magnetic field is applied in the [001] direction, the attenuation is characterized by four peaks,

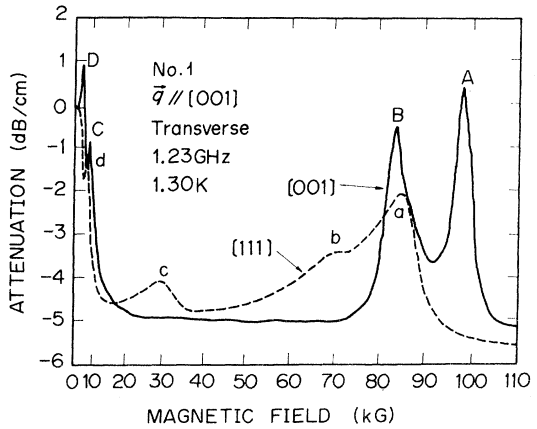

FIG. 3. Magnetic field dependences of the attenuation of the 1.23-GHz transverse waves propagating along the [001] direction in sample No. 1 at 1.3 K. The acoustic-power level was 0.006 mW/cm^2. The Miller indices attached to the lines indicate the direction of the magnetic field. The resonance peaks are denoted by A, B, C, and D for $\vec{H}$ || [001], and by a, b, c, and d for $\vec{H}$ || [111].

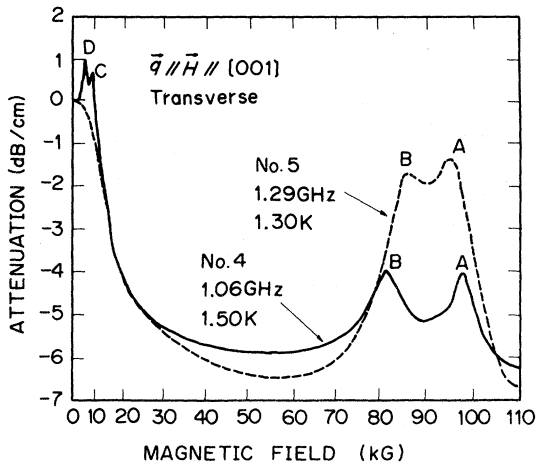

FIG. 4. Magnetic field dependences of the attenuation of the transverse waves propagating along the [001] direction in sample Nos. 4 (solid line) and 5 (broken line). The magnetic field was applied in the [001] direction. The experimental conditions are attached to the lines. The acoustic-power levels were 1 and 0.1 mW/cm^2 in sample Nos. 4 and 5, respectively. The peaks denoted by *A*, *B*, *C*, and *D* correspond to the resonance peaks assigned by the same letters in Fig. 3.

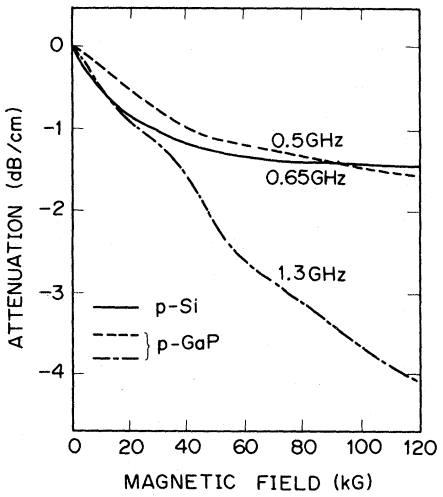

FIG. 5. Magnetic field dependences of the attenuation at 4.2 K in B-doped Si (solid line) and Zn-doped GaP (broken lines). The attenuations in the absence of the magnetic field are set to 0 dB. The acoustic frequencies are denoted to the lines.

A, *B*, *C*, and *D*. When the magnetic field is applied in the [111] direction, the attenuation shows four peaks *a*, *b*, *c*, and *d* at different fields from the above. We regard these peaks as the resonance-attenuation peaks, since they appear in the limited-field region, shift with the acoustic frequency, and saturate with increasing the acoustic power. The background attenuation rapidly decreases up to 20–30 kG and then is almost constant up to 120 kG. The overall behavior of the magnetic field dependence is similar in sample Nos. 4 and 5 as shown in Fig. 4.

We show that these resonance behaviors are specific to the attenuation by the acceptor holes in germanium.[32] We could observe the MARA in neither B-doped Si nor Zn-doped GaP, although we could observe the attenuation by the acceptor holes which are characterized by the increase with decreasing the temperature below 20 K. In Fig. 5 are shown the magnetic field dependence of the attenuation in these two samples. In B-doped Si (the sample Si16LD in Ref. 24), the attenuation decreases rapidly up to 40 kG and then decreases gradually up to 120 kG. In Zn-doped GaP (~1.5×10^{17} cm^{-3}), the attenuation decreases monotonically up to 120 kG. These magnetic field dependences in *p*-Si and *p*-GaP look like the background attenuation in *p*-Ge.

In later sections, we describe the MARA in Ga-doped Ge. In the present investigation, we concentrate our attention to the resonance-attenuation peaks at high magnetic fields (>30 kG), in order to make possible to compare with the theory (Sec. V). We found that the MARA varied with both the temperature and the acoustic power, reflecting the attenuation in the absence of the magnetic field (Sec. IV A). However, it turned out that the resonance-peak positions are affected by neither the temperature nor the acoustic power. We show that the MARA changes with the acoustic frequency, the acoustic mode, the magnetic field direction, and the uniaxial stress.

1. Acoustic-power dependence

When we changed the acoustic power, the resonance-peak attenuations were affected but shifts in the resonance-peak positions were not observed. Figure 6 shows the effect of the acoustic power on the MARA in sample No. 2. The bottom line represents the MARA at 6 mW/cm^2 and the attenuation peaks are faint. The successive lines upwards represent the MARA obtained with decreasing the acoustic power. As the acoustic power was decreased, the attenuations of the peaks *A* and *B* were increased. However, the resonance-peak positions did not shift appreciably with the acoustic power. These behaviors of the acoustic-power dependence of the MARA were found at any temperatures below 4.2 K and in the other samples.

The acoustic-power dependence of the MARA is related to the saturation effect described in Sec. IV A and will be discussed in Sec. V C. In Secs. IV B 2–IV B 7, our measurements were performed

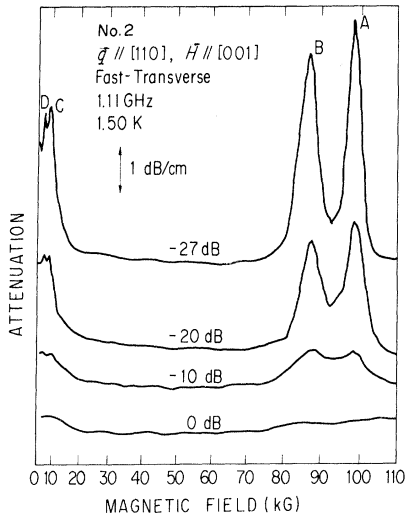

FIG. 6. Acoustic-power dependence of the MARA of the 1.11-GHz fast transverse waves propagating along the [110] direction in sample No. 2 at 1.5 K. The magnetic field was applied in the [001] direction. The scale of the ordinate is indicated by an arrow representing 1 dB/cm. Numerals attached to the lines show the acoustic-power levels in unit of dB; 0 dB corresponds to 6 mW/cm^2. The peaks denoted by A, B, C, and D correspond to the resonance peaks assigned by the same letters in Fig. 3.

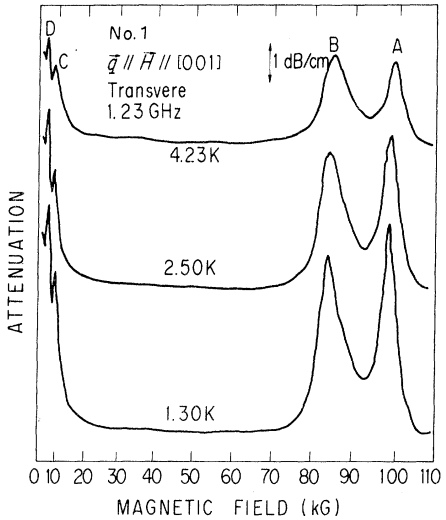

FIG. 7. Temperature dependence of the MARA of the 1.23-GHz transverse waves propagating along the [001] direction at 0.06 mW/cm^2 in sample No. 1. The magnetic field was applied in the [001] direction. The scale of the ordinate is indicated by an arrow representing 1 dB/cm. The peaks denoted by A, B, C, and D correspond to the resonance peaks assigned by the same letters in Fig. 3.

in the low acoustic power where the signal is clear enough to follow the detailed behavior. Our analysis which is related to the determination of the Zeeman-splitting parameters of the acceptor ground state is carried out in relation to the resonance-peak positions, which are not affected appreciably by the acoustic power.

2. *Temperature dependence*

When the temperature was varied, the resonance-peak attenuations were changed appreciably but the resonance-peak positions were affected little. Figure 7 shows the effect of the temperature on the MARA in sample No. 1 under $\vec{H}||[001]$. The successive lines upwards represent the MARA obtained with increasing the temperature. As decreasing the temperature, the attenuations of the peaks A and B increased appreciably but the resonance-peak positions shifted little. The similar temperature dependences were found for the other modes and samples.

3. *Acoustic-frequency dependence*

When the acoustic frequency was changed, the resonance-peak positions were shifted. In Fig. 8 is shown the acoustic-frequency dependence of the MARA in sample No. 2 under $\vec{H}||[001]$. The successive lines downwards represent the MARA with decreasing the acoustic frequency. As decreasing the frequency, the resonance-peak positions shifted appreciably; the peak A shifted toward lower magnetic fields and the peak B shifted toward higher magnetic fields with decreasing the frequency. At 0.58 GHz, two resonance peaks could

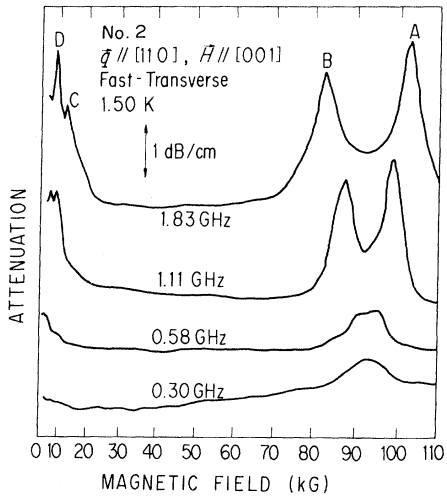

FIG. 8. Acoustic-frequency dependence of the MARA of the fast transverse waves propagating along the [110] direction in sample No. 2 at 1.5 K under $\vec{H}||[001]$. The scale of the ordinate is indicated by an arrow representing 1 dB/cm. The acoustic power levels are not the same for all cases. The peaks denoted by A, B, C, and D correspond to the peaks assigned by the same letters in Fig. 3.

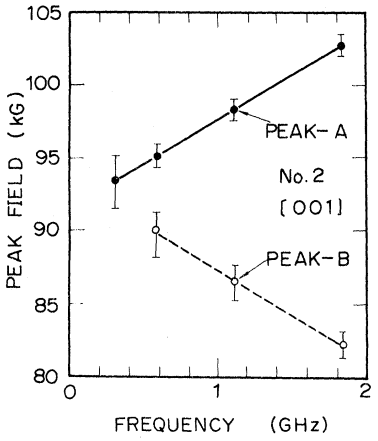

FIG. 9. Acoustic-frequency dependence of the resonance-peak fields for the case of Fig. 8.

not be observed separately. Below 0.30 GHz, we could observe one peak at high magnetic fields.

The feature of the resonance-peak shift with the acoustic frequency is shown in Fig. 9. The peak A shifts almost linearly toward lower magnetic fields, whereas the peak B toward higher magnetic fields with decreasing the acoustic frequency. Consequently, these peaks approach each other with decreasing the frequency and overlap near 92 kG. When the magnetic field was applied in the [111] direction, the peaks a and b shift similarly to the peaks A and B, respectively, with the acoustic frequency.

We do not show the acoustic frequency dependence of the resonance-peak attenuations, since we could not observe the attenuation by controlling the degree of saturation.

4. *Acoustic-mode dependence*

The MARA changes with the acoustic mode in both the magnitude and the peak positions. This reflects the difference in the coupling parameters or the selection rules. Figure 10 shows the MARA of the 1.83-GHz fast transverse waves and of the 1.84-GHz longitudinal waves propagating along the [110] direction in sample No. 2. For the transverse waves, the MARA is quite similar to the solid line in Fig. 3. On the other hand, for the longitudinal waves, the feature of the MARA is quite different from that of the transverse waves; peaks A and B were not observed, but two clear resonance peaks were found near 18 and 46 kG.

5. *Magnetic-field-direction dependence*

When the sample was rotated so that the magnetic field was rotated from the [001] to the [111] direction in the $(1\bar{1}0)$ plane, we found shifts in the resonance-peak positions. Figure 11 shows the

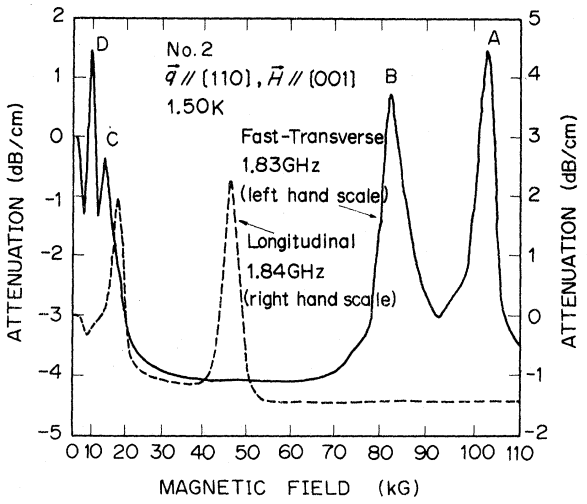

FIG. 10. Magnetic field dependence of the attenuations of both the 1.83-GHz fast transverse waves (solid line) and the 1.84-GHz longitudinal waves (broken line) propagating along the [110] direction in sample No. 2 at 1.5 K and at 0.06 mW/cm^2. The magnetic field was applied in the [001] direction. The peaks denoted by A, B, C, and D correspond to the peaks assigned by the same letters in Fig. 3.

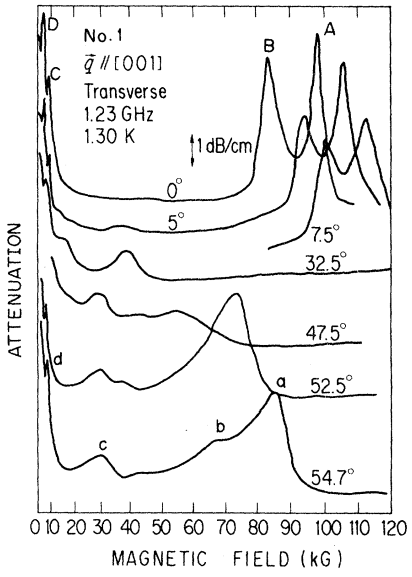

FIG. 11. Magnetic field direction dependence of the MARA of the 1.23-GHz transverse waves propagating along the [001] direction in sample No. 1 at 1.3 K. Numerals attached to the lines denote angles in unit of degrees between the [001] direction and the magnetic field in the $(1\bar{1}0)$ plane. The acoustic power levels are not the same for all cases. The peaks denoted by A, B, C, and D at 0° and by a, b, c, and d at 54.7° correspond to the peaks assigned by the same letters in Fig. 3.

MARA in sample No. 1 for the 1.23-GHz transverse waves at several magnetic field directions. The [001] and the [111] directions correspond to 0° and 54.7°, respectively. Thus, peaks A, B, C, and D for 0° and a, b, c, and d for 54.7° were observed in accordance with Fig. 3. The successive lines downwards from the line for 0° represent the MARA with increasing θ, which is an angle from the [001] direction. The resonance-peak positions are strongly affected by the magnetic field direction.

In Fig. 12 is shown the magnetic-field-direction dependences of the resonance-peak positions observed in sample No. 1 for the 1.23-GHz transverse waves. When the magnetic field was set in the [001] direction, four peaks A, B, C, and D were found. The peaks A and B move toward higher magnetic fields with increasing θ slightly. When $\theta > 10°$, these peaks could not be found in magnetic fields up to 120 kG. Following the disappearance of the high magnetic field peaks, two peaks were found at low magnetic fields (near 20 and 40 kG). The low-field peaks did not shift appreciably as θ increased from 10° to 40°. When $40° < \theta < 70°$, the low-field peaks shifted toward higher magnetic fields making the maximum near 55°. At 54.7°, the peak at 40 kG may be connected to the peaks a or b and the peak at 20 kG to the peak c.

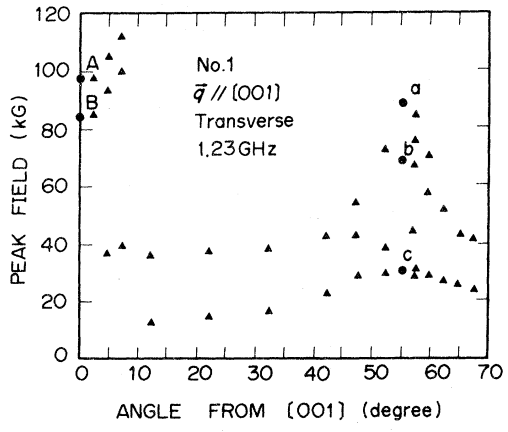

FIG. 12. Magnetic field direction dependence of the resonance fields for the case of Fig. 11. Circles denoted by A and B at 0° and by a, b, and c at 54.7° correspond to the peaks in Fig. 3. Triangles denote the peaks at the other angles.

6. *Uniaxial-stress dependence*

When we applied the uniaxial stress, the shifts in the resonance-peak positions were observed at rather weak stress. Sample No. 3 was prepared for this experiment so that both the compressional stress and the magnetic field were applied in the [001] direction. The 1.11-GHz fast transverse waves were propagated along the [110] direction at 4.2 K.

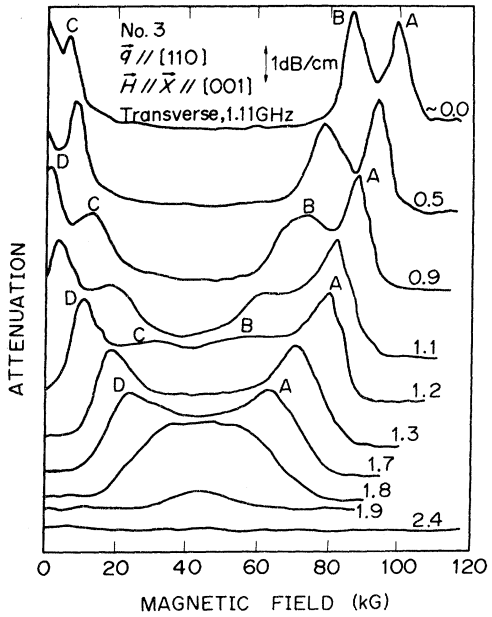

FIG. 13. Uniaxial compressional stress dependence of the MARA of the 1.11-GHz fast transverse waves propagating along the [110] direction in sample No. 3 at 4.2 K and the acoustic-power level of 0.06 mW/cm^2. Both the magnetic field and the uniaxial stress were applied along the [001] direction. Numerals attached to the lines denote the magnitudes of the uniaxial stress in unit of 10^7 dyn/cm^2. The scale of the ordinate is indicated by an arrow representing 1 dB/cm. The peaks denoted by A, B, C, and D correspond to the peaks assigned by the same letters in Fig. 3.

Figure 13 shows the effect of the uniaxial stress on the MARA. The top line represents the MARA in the absence of the stress. The successive lines downwards represent the MARA with increasing the stress. As increasing the stress, the peaks A and B shift toward lower magnetic fields and the peaks C and D toward higher magnetic fields. At ~1.8×10^7 dyn/cm^2, the peaks overlap near 45 kG. Above 2.4×10^7 dyn/cm^2, we could observe no peaks in magnetic fields up to 120 kG.

7. *Acceptor-concentration dependence*

The resonance-peak positions were not affected by the acceptor concentration remarkably in the adopted samples, when the acoustic mode and the magnetic field direction were the same. The MARA obtained in three samples with different concentrations by using the transverse waves propagating along the [001] direction under

$\vec{H}||[001]$ are shown in Figs. 3 and 4. The resonance-peak positions did not shift remarkably but the resonance-peak widths were broadened with increasing the acceptor concentration. The peaks A and B became obscure and the peaks C and D became faint with increasing the concentration. We cannot compare the resonance-peak attenuations rigorously, since the degrees of the saturation effect are not the same for three cases.

V. ANALYSES OF EXPERIMENTAL RESULTS

A. Magnetoacoustic resonance attenuation

The attenuation coefficient (3.2) consists of two terms: one is the resonance term and another the relaxation term which exists when $|C_{\vec{q}t}^{nn}|^2 \neq 0$ ($n = 1, 2, 3, 4$). When the attenuation is measured as a function of the magnetic field, the resonance absorption of the ultrasonic waves is observed at the fields where $E_{n'n} = \hbar\omega$ ($n \neq n'$). The magnitude of the resonance attenuation is proportional to $1/(\Gamma_n + \Gamma_{n'})$, where n and n' denote the levels relevant to the resonance process. Since Γ_n decreases with decreasing the temperature as will be described in Sec. V B, the attenuation is expected to increase with decreasing the temperature. When the value of Γ_n is small, the saturation effect appears. However, since both the temperature and the acoustic power do not affect the resonance fields, we can disregard this effect in the consideration of the energy splittings of the acceptor ground state. The resonance fields change with the acoustic frequency, the magnetic field direction, and the uniaxial stress as described in Sec. IV B.

It should be noted that the theory and formulas described in Sec. III are useful under the strong magnetic field where the axis of quantization of the system can be taken along the magnetic field direction. Thus we will carry out the comparison of the experimental results with the theory above 30 kG.

1. Comparison of the observed resonance fields with the theory

In order to find the resonance fields, we calculate the magnetic field dependence of the energy splitting $E_{n'n}$. We consider first two cases where the magnetic field is applied in either the [001] or the [111] direction. In these two cases, the acceptor ground state is well represented by the state for the angular momentum $J = \frac{3}{2}$ and the formulas are simplified as described in Sec. III.

We take account of the following factors: the selection rules in the coupling of the ultrasonic waves with the acceptor holes, the acoustic-frequency dependence of the MARA, and the uniaxial-stress dependence of the MARA. The selection rules are derived from Refs. 27 and 28.[36] For $\vec{H}||[001]$, the hole transitions between levels 1 and 2 and between levels 3 and 4 are allowed for both the transverse waves propagating along the [001] direction and the fast transverse waves propagating along the [110] direction. Moreover the transitions between levels 1 and 3 and between levels 2 and 4 are allowed for the longitudinal waves propagating along the [110] direction. For $\vec{H}||[111]$, all transitions are allowed for both the transverse and the longitudinal waves propagating along the [001] direction. Based on these selection rules, the allowed resonance transitions are related to the observed peaks under $\vec{H}||[001]$ as follows: For the peaks A and B,

$$|E_{12}| = \hbar\omega \tag{5.1}$$

or

$$|E_{43}| = \hbar\omega\,, \tag{5.2}$$

and, for the peak near 46 kG in Fig. 11,

$$|E_{13}| = \hbar\omega \tag{5.3}$$

or

$$|E_{42}| = \hbar\omega\,, \tag{5.4}$$

where the expressions for $E_{n'n}$ are given in Appendix A.

In addition to these resonance conditions, we take the uniaxial stress dependence of the levels into account. When the stress $\vec{X}$ is applied in the [001] direction, the acceptor ground state splits as

$$\Delta(X) = \tfrac{4}{3} D_u^a (S_{11} - S_{12}) X \equiv \zeta X \quad (\zeta > 0)\,, \tag{5.5}$$

where S_{11} and S_{12} are cubic compliance constants, and $\zeta > 0$ indicates that the $|\frac{3}{2}\rangle$ states are higher than the $|\frac{1}{2}\rangle$ states in energy.

First we consider the case of $\vec{H}||[001]$. Since we try to determine the parameters g_1', g_2', q_2, q_3, and Δ_0, which are included in the expressions for $E_{n'n}$, it is necessary to take four cases for each resonance conditions, (5.1) or (5.2)

$$\begin{aligned}
&\text{(a)}\ \ q_2 + q_3 > 0 \ \text{ and } \ g_1' + \tfrac{13}{4} g_2' > 0\,;\\
&\text{(b)}\ \ q_2 + q_3 > 0 \ \text{ and } \ g_1' + \tfrac{13}{4} g_2' < 0\,;\\
&\text{(c)}\ \ q_2 + q_3 < 0 \ \text{ and } \ g_1' + \tfrac{13}{4} g_2' > 0\,;\\
&\text{(d)}\ \ q_2 + q_3 < 0 \ \text{ and } \ g_1' + \tfrac{13}{4} g_2' < 0\,.
\end{aligned} \tag{5.6}$$

From the consideration in Appendix B, the four cases for each resonance transition are reduced to one as

(i) the case (b) for (5.1)

and (5.7)

(ii) the case (a) for (5.2).

Further we take account of transitions (5.3) and (5.4). When we take (5.3), the linear Zeeman-splitting parameters are obtained by the least-squares fits of the calculations to the observed behavior of the MARA as follows:

(I) $g_1' = 2.75$ and $g_2' = -1.58$ for the case (i) in (5.7);

(II) $g_1' = -0.16$ and $g_2' = 0.08$ for the case (ii) in (5.7).

When we take (5.4), the following linear Zeeman parameters are obtained by the same procedure:

(III) $g_1' = 0.43$ and $g_2' = -1.60$ for the case (i) in (5.7);

(IV) $g_1' = -0.08$ and $g_2' = 0.06$ for the case (ii) in (5.7).

The quadratic Zeeman-splitting parameter for the above four cases is the same as $q_2 + q_3 = 0.44 \times 10^{-5}$ K/kG^2. A further reduction in the number is allowed when we take account of the observations for $\vec{H} \| [111]$.

Since all transitions are allowed for $\vec{H} \| [111]$ described above, we take the way to calculate the energy splittings $E_{n'n}$ by using the values obtained for each case and then to compare those with the observations for $\vec{H} \| [111]$. Consequently, it turned out that only one case, (II), is adequate to explain the observed frequency dependence consistently, whose feature is shown in Figs. 14 and 15 for $\vec{H} \| [001]$ and $\vec{H} \| [111]$, respectively. The values of the five parameters obtained are listed in Table III.

2. *Magnetic-field-direction dependence of the resonance fields*

We can explain the magnetic-field-direction dependence of the resonance fields by using the parameters derived in Sec. V A 1. We consider the case where the magnetic field is rotated from the [001] to the [111] direction in the $(1\bar{1}0)$ plane. We choose the magnetic field direction as the axis of quantization of the system under strong magnetic fields.

For an arbitrary direction of the magnetic field, the Zeeman Hamiltonian is written[40]

$$
\begin{aligned}
H_{\text{Zeeman}} = \mu_B \Big[& g_1' \Big(\frac{1}{\sqrt{2}} \sin\theta (J_x + J_y) + \cos\theta J_z \Big) \\
& + g_2' \Big(\frac{1}{\sqrt{2}} \sin\theta (J_x^3 + J_y^3) + \cos\theta J_z^3 \Big) \Big] H \\
& + \Big[q_1 + q_2 \Big(\frac{1}{\sqrt{2}} \sin\theta (J_x + J_y) + \cos\theta J_z \Big)^2 \\
& + q_3 \big(\tfrac{1}{2} \sin^2\theta (J_x^2 + J_y^2) + \cos^2\theta J_z^2 \big) \Big] H^2 ,
\end{aligned}
\tag{5.8}
$$

where θ is the angle from the [001] direction. We can obtain the energies of the Zeeman sublevels by diagonalizing this Hamiltonian matrix. We calculated the energies numerically by using a computer under two assumptions: $q_1 = 0$ K/kG^2 and $\Delta_0 = 0$ K. Since q_1 is canceled out in the calculation of $E_{n'n}$, the assumption of $q_1 = 0$ K/kG^2 is harmless.

Figure 16 shows the calculated magnetic field dependences of the Zeeman sublevels for $\vec{H} \| [001]$ and $\vec{H} \| [111]$. For $\vec{H} \| [001]$, levels 3 and 4 cross near 84 kG. Then the resonance condition (5.2) is satisfied at both sides of its crossing, which are shown by broken arrows with T, for the 1.83-GHz fast transverse waves propagating along the [110] direction. Broken arrows with L show the allowed transitions for the 1.84-GHz longitudinal waves

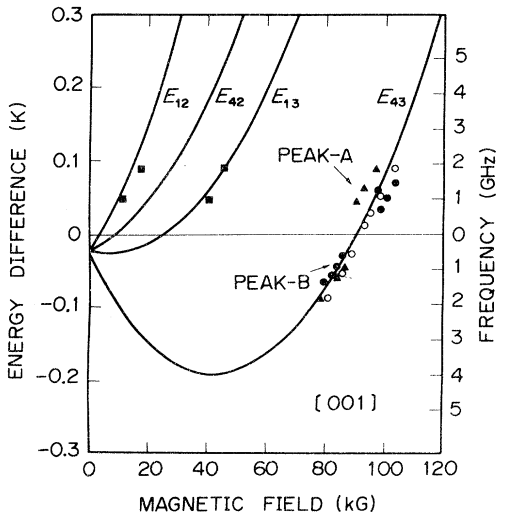

FIG. 14. Calculated magnetic field dependences of the energy differences $E_{nn'}$ for $\vec{H} \| [001]$ and $X = 0$. The ordinate is expressed in two ways: The left scale is in units K. The right scale is in GHz for plotting the observed frequency dependence of the resonance-peak fields. Closed circles and triangles represent the transverse and the longitudinal waves, respectively, propagating along the [001] direction in sample No. 1. Open circles and closed rectangles represent the fast transverse and the longitudinal waves, respectively, propagating along the [110] direction in sample No. 2.

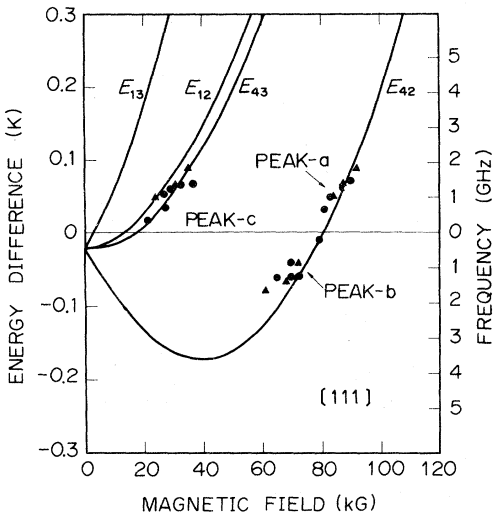

FIG. 15. Calculated magnetic field dependences of the energy differences $E_{nn'}$ for $\vec{H}\|[111]$. The ordinate is the same as Fig. 14. Closed circles and triangles represent the transverse and the longitudinal waves, respectively, propagating along the [001] direction in sample No. 1.

propagating along the [110] direction. Solid arrows show the allowed transitions for the 1.23-GHz transverse waves propagating along the [001] direction (hereafter this wave is considered). For $\vec{H}||[111]$, levels 2 and 4 cross near 80 kG and the transitions are allowed at both sides of 80 kG as shown by solid arrows. Moreover, two allowed transitions exist in low magnetic fields as shown by solid arrows.

When the magnetic field is rotated from the [001] to the [111] direction by 5°, 30°, 50°, and 60°, the calculated magnetic field dependences of the Zeeman sublevels are shown in Fig. 17. In these cases, the movements of the levels with the magnetic field are different a little from the above two cases (Fig. 16). When two levels approach each other, the level anticrossing occurs due to the mixing of the $|M_J\rangle$ states.[36] At 5°, the splitting energy due to the anticrossing is smaller than the ultrasonic wave energy and the resonance condition allows four transitions as shown by solid arrows. Two arrows in high magnetic fields shift toward

TABLE III. Parameters of the acceptor ground state obtained from the MARA.

Δ_0	-0.02 ± 0.006 K
g_1'	-0.16 ± 0.08
g_2'	0.08 ± 0.04
q_2	$(0.5\pm0.2)\times10^{-4}$ K/kG^2
q_3	$-(0.6\pm0.2)\times10^{-5}$ K/kG^2
σ	0.03 K (sample Nos. 1 and 4)
	0.05 K (sample No. 5)

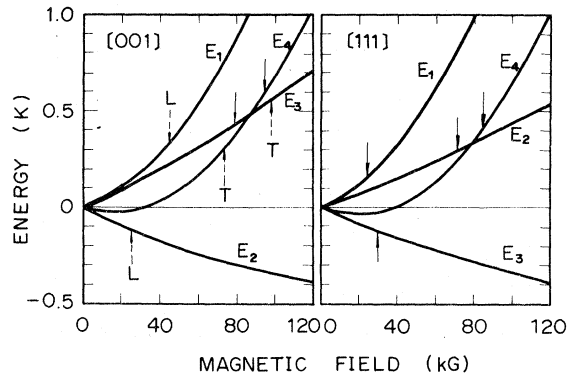

FIG. 16. Calculated magnetic field dependences of the energies E_n ($n=1,2,3,4$) of the Zeeman sublevels for $\vec{H}\|[001]$ and $\vec{H}\|[111]$. The resonance transitions are indicated by arrows: Solid arrows with no letters correspond to the 1.23-GHz transverse waves propagating along the [001] direction; broken arrows denoted by the letters T and L correspond to the 1.83-GHz fast transverse waves and the 1.84-GHz longitudinal waves, respectively, propagating along the [110] direction.

higher magnetic fields than those for $\vec{H}||[001]$. Two transitions in low magnetic fields, which are forbidden for $\vec{H}||[001]$, are allowed in the present case. When θ increases to 30°, the resonance condition in high magnetic fields is not satisfied below 120 kG but two transitions in low magnetic fields are allowed, whose positions shift little from those for 5°. For 50° and 60°, the

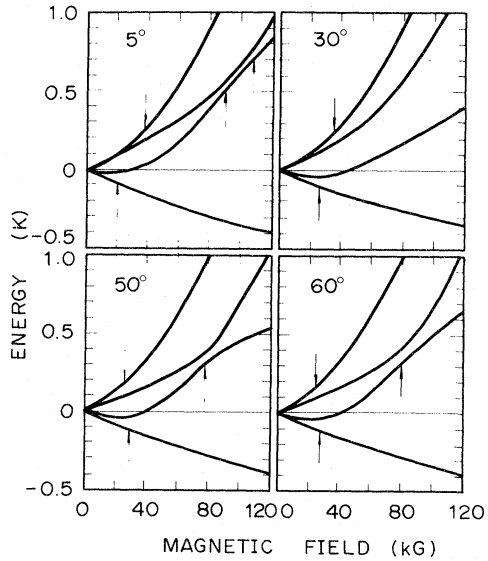

FIG. 17. Calculated magnetic field dependences of the energies of the Zeeman sublevels for the cases $\theta=5°$, 30°, 50° and 60° (θ is the angle between the [001] direction and the magnetic field in the $(1\bar{1}0)$ plane). Arrows indicate the resonance field correspond to the 1.23-GHz transverse waves propagating along the [001] direction.

feature of the magnetic field dependence is similar to each other and the anticrossing occurs near 80 kG. The splitting energy is comparable with the ultrasonic-wave energy and hence only one transition is allowed in high magnetic fields. In low magnetic fields, two transitions are allowed as the cases for 5° and 30°.

The above calculated results agree well with the observations in Fig. 12. So far, we assumed $\Delta_0 = 0$ K, which is inconsistent with the results in Sec. V A 1. However, since Δ_0 is about −0.02 K, the introduction of Δ_0 changes only slightly the level diagrams in Figs. 16 and 17.

B. Temperature and magnetic field dependences of the level widths Γ_n

To calculate the coupling of the ultrasonic waves with the acceptor holes, we use the deformation-potential constants obtained by piezospectroscopy.[42] On the other hand, in the calculation of the level widths Γ_n, we adopt the "dynamic" deformation-potential constants determined by the heat-pulse experiment[28] by the following facts: (i) We cannot explain the relaxation-attenuation peak near 7 K (Fig. 2) by taking the deformation-potential constants derived by the piezospectroscopy.[36] (ii) Γ_n are determined by the phonons which are in the same frequency range as the phonons contained in the heat pulse. (iii) The analysis of the heat-pulse data stands basically on the same principle adopted here. Moreover, since it is assumed in the derivation of the ultrasonic attenuation formulas in Sec. III that the envelope functions consist of solely s-like parts, the deformation-potential constants for the acceptors become equal to those for the valence-band edge.[21] Thus, we use the deformation-potential constants of $D_u^a = 5.45$ eV and $D_{u'}^a = 6.10$ eV for Γ_n,[28] whereas $D_u^a = 3.32$ eV and $D_{u'}^a = 3.81$ eV for the coupling of the ultrasonic waves with the acceptor holes.[42]

First, we calculate the temperature dependence of the level widths Γ_n in the absence of the magnetic field. Figure 18 shows the calculated temperature dependence of Γ_R $(=\Gamma_{Rn}, n=1,2,3,4)$, Γ_1^d $(=\Gamma_4^d)$, and Γ_2^d $(=\Gamma_3^d)$ under the assumption that the splitting is uniform throughout the sample. For $\Delta = -0.02$ K, Γ_n^d are smaller than those for $\Delta = -0.1$ K by one or more orders at any temperatures. Thus, the contribution of Γ_n^d to the level width is negligibly small and that of Γ_R dominates. Now we consider the attenuation of the 1.11-GHz ultrasonic waves. Γ_R near 12 K becomes equal to the energy corresponding to 1.11 GHz as shown in Fig. 18 and then the Lorentzian in the attenuation formula (3.2) has a maximum value. Since the relaxation attenuation includes the terms N_1, N_2, and

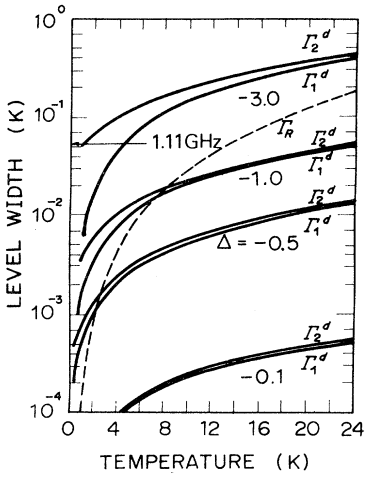

FIG. 18. Calculated temperature dependences of the level width Γ_R $(=\Gamma_{Rn}, n=1,2,3,4)$, Γ_1^d $(=\Gamma_4^d)$, and Γ_2^d $(=\Gamma_3^d)$ as functions of the uniform splitting Δ. The value of Δ is represented in units of K. The arrow mark denotes the temperature corresponding to 1.11 GHz.

$1/T$, in addition to the Lorentzian,[19] the resultant temperature dependence shows the maximum near 7.3 K. This is consistent with the observations. Below 4.2 K, where the MARA was observed, the relaxation attenuation is small.

When the magnetic field is applied in the [001] direction, Γ_n^d $(n=1,2,3,4)$ increase with increasing the magnetic field as shown in Fig. 19. The level widths are determined by Γ_R below 30 kG and is

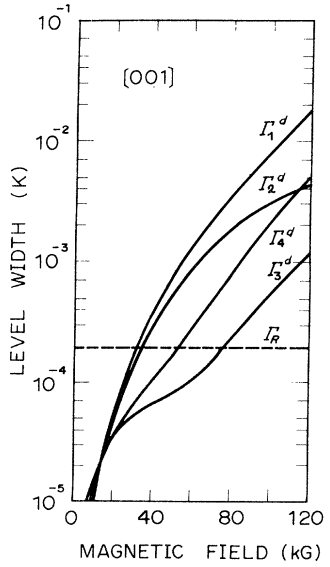

FIG. 19. Calculated magnetic field dependences of the level widths Γ_n^d $(n=1,2,3,4)$ due to the direct process and $\Gamma_{Rn}=\Gamma_R$ $(n=1,2,3,4)$ due to the Raman process at 1.3 K for $\tilde{H} \parallel [001]$.

$\sim 2 \times 10^{-4}$ K. Above 30 kG, the contribution of Γ_n^d to the level widths dominates since Γ_n^d increase with increasing the magnetic field. The similar results are obtained for $\vec{H} \| [111]$.[36]

C. Saturation effect in the ultrasonic attenuation

The resonance process may be suppressed by the saturation effect: As increasing the acoustic power, the lower level becomes more depopulated and hence the attenuation saturates. When the relaxation time of the two-level system is long, the acoustic-power level causing the saturation is lowered.

When we consider first that the two-level system is localized mutually, the acoustic-power, P, dependence of the ultrasonic resonance attenuation is expressed by[43]

$$\alpha_{\text{resonance}} = \alpha_0 (1 + P/P_c)^{-1}, \tag{5.9}$$

where α_0 is the unsaturated attenuation and P_c the critical acoustic power, which is inversely proportional to the relaxation time.

In the absence of the magnetic field, the acoustic-power dependences of the attenuations at 1.5 and 4.2 K in sample No. 2 are shown in Fig. 20. The attenuations are obtained by subtracting the residual attenuations from Fig. 1. As described in Sec. V B, the attenuations at low temperatures in Fig. 20 are mostly ascribed to the resonance process. In the presence of the magnetic field, the acoustic power dependences of the resonance attenuations of the peaks A and B at two temperatures (4.2 and 1.5 K) in sample No. 2 are shown in Fig. 21. The resonance attenuations are defined as the differences between the peak attenuations and the background ones.

When we take the most probable fitting of Eq. (5.9) to the experimental results in these figures, the solid lines are obtained and then α_0 and P_c are also obtained as listed in Table IV. The critical acoustic power P_c's in the absence and the presence of the magnetic field are almost the same. Since Γ_n in the absence of the magnetic field is much smaller than one near 100 kG as shown in Fig. 19 it is expected that P_c in the absence of the magnetic field is much smaller than one near 100 kG. This does not agree with the experimental results in which two P_c's are similar. This indicates that the other interaction causing the level broadening exist in addition to both the direct and the Raman processes: for example, the transverse relaxation mechanism due to the interaction among the acceptor impurities as in the amorphous materials.[44]

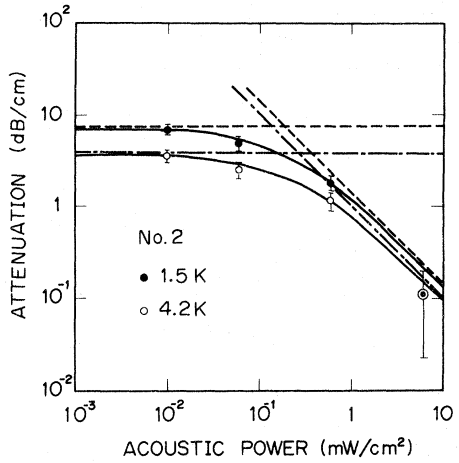

FIG. 20. Acoustic-power dependences of the attenuations at 1.5 K (closed circles) and at 4.2 K (open circles) for the case of Fig. 1. Solid lines indicate the least-squares-fitted lines of Eq. (5.9). Broken lines indicate asymptotic lines in extreme cases ($P \ll P_c$, and $P \gg P_c$).

D. Acceptor-concentration dependence: Line shapes

The resonance fields are almost the same for three samples with different concentrations as shown in Figs. 3 and 4, when we take account of those shifts due to the difference of the acoustic frequency. However, the line shape of the MARA changes with the acceptor concentration. We assume that the resonance linewidth is due to the distributed initial splittings. Then we try to fit the line shapes by varying the initial splittings. We take

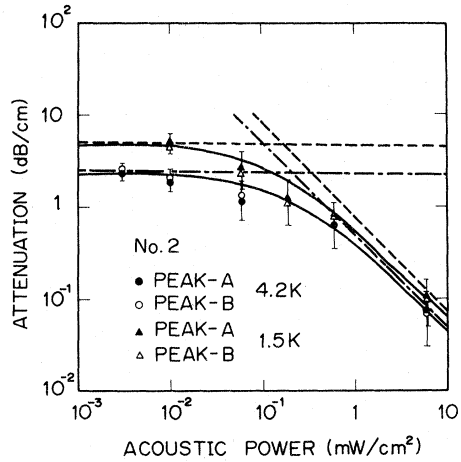

FIG. 21. Acoustic-power dependences of the resonance-peak attenuations at 1.5 K (triangles) and at 4.2 K (circles) for the case of Fig. 6. Solid lines indicate the least-squares-fitted lines of Eq. (5.9). Broken lines indicate asymptotic lines in extreme cases ($P \ll P_c$ and $P \gg P_c$).

TABLE IV. Unsaturated attenuation α_0 and critical acoustic power P_c in sample No. 2.

T (K)	α_0 (dB/cm)	P_c (mW/cm^2)
(a) In the absence of the magnetic field		
1.5	7.1	0.19
4.2	3.6	0.27
(b) MARA		
1.5	3.9	0.17
4.2	2.2	0.22

up the resonance line shapes of the peaks A and B, since their shapes are clear.

Figure 22 shows the calculated line shapes for sample No. 1. The scaling factor β (Appendix A) is adjusted so that the resonance-peak attenuation coincides with the experimental: $\beta = 0.29$ for sample No. 1. When σ is taken to be 0.02, 0.03, and 0.04 K, the calculated line shape is varied as shown in Fig. 22. A good fitting to the observation (Fig. 3) is obtained for $\sigma = 0.03$ K. In sample Nos. 4 and 5, the calculations with $\sigma = 0.03$ and 0.05 K, respectively, are the best fits to the observations (Fig. 4). These are listed in Table III. If the value of Δ_0 is changed, the resonance fields shift and then the calculated value becomes inconsistent with the observation.

E. Temperature dependence

When the resonance condition is satisfied, the resonance-peak attenuation is proportional to $1/(\Gamma_n + \Gamma_{n'})$ as described previously. Since Γ_n changes with both the temperature and the magnetic field, the peak attenuation changes with these parameters. To compare the numerical calculation with the observed temperature dependence of the MARA, we take account of the distributed initial splittings estimated by the line-shape fitting.

Figure 23 shows the calculated temperature dependences of the resonance attenuations of the peaks A (solid lines) and B (broken lines) in sample No. 1 under $\vec{H} \| [001]$. Groups of the lines AL and AH are obtained by fitting the calculations to the data of the peak A at 1.3 and 4.2 K, respectively. Then the scaling factor β is 0.37 for the line AL and 0.67 for the line AH. All of the observed attenuations lie between the lines AL and AH; the scaling factor decreases with decreasing the temperature. This is ascribed to the saturation effect, which is more probable at the lower temperatures reflecting the decrease of the level width.

In Fig. 24 is shown the calculated attenuation in the absence of the magnetic field. This figure indicates that the relaxation attenuation becomes negligible below 4.2 K and the attenuations are mostly due to the resonance process as described previously. We should remark here that the calculated level widths at low temperatures become too small in the absence of the magnetic field as discussed in Sec. V C. Since we have no tractable

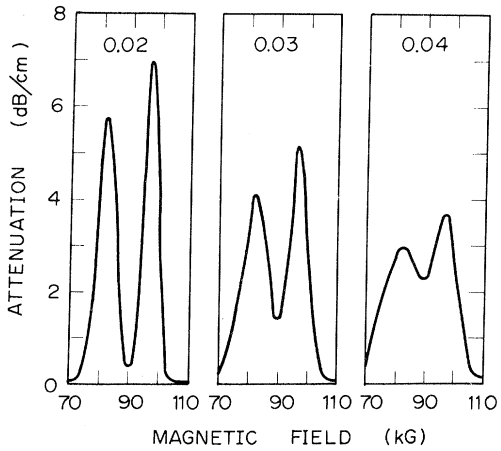

FIG. 22. Calculated magnetic field dependences of the attenuation for the case of Fig. 3 (solid line) in the range 70–110 kG. Inserted decimals indicate the values of σ in units of K. The scaling factor β is 0.29.

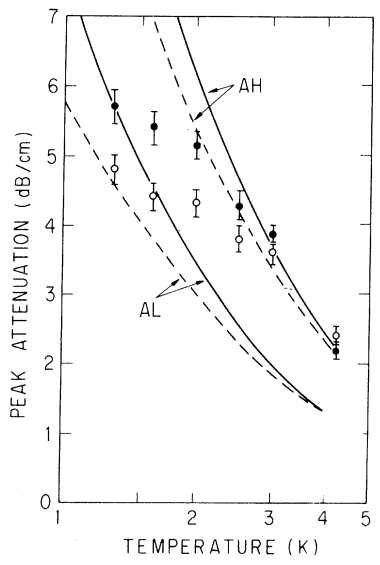

FIG. 23. Calculated temperature dependences of the resonance-peak attenuations of the 1.23-GHz transverse waves propagating along the [001] direction in sample No. 1. Solid and broken lines show the attenuations for the peaks A and B, respectively. Closed and open circles show the data for the peaks A and B, respectively. Groups of the lines AL and AH represent the fitted lines to the data at 1.3 and 4.2 K, respectively. In these calculations, $\Delta_0 = -0.02$ K and $\sigma = 0.03$ K are used and the scaling factor β is 0.37 for AL and 0.67 for AH.

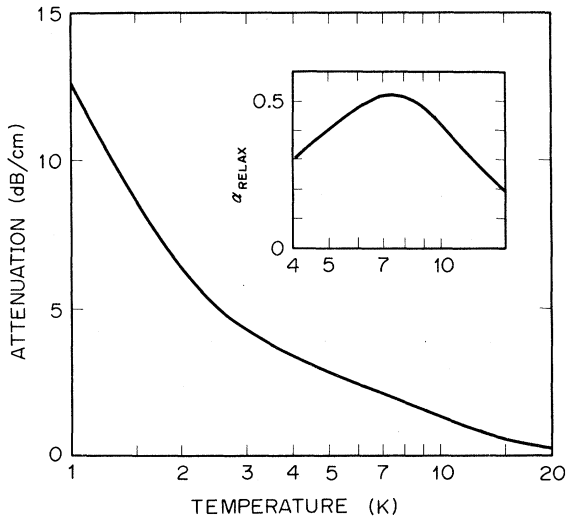

FIG. 24. Calculated temperature dependences of the attenuation of the 1.11-GHz fast transverse waves propagating along the [110] direction in sample No. 2. Inset shows the relaxation attenuation in the range 4–15 K. In the calculation the following values are used: $\beta_1 = \beta_2 = 1$, $\Delta_0 = -0.02$ K, and $\sigma = 0.03$ K.

way to consider other relaxation processes, we calculated the temperature dependence of the attenuation by ignoring it.

VI. DISCUSSION

A. Linear Zeeman effect

We attempted first to explain the MARA by using the g values derived from the magneto-optical absorption by SF.[33,32] However, we found that these values were not adequate to explain the MARA consistently. As described in Sec. V A, we derived the g values to explain the observed behaviors of the MARA.

It is clear that SF's and ours are different beyond the error or the chemical effects. To resolve this problem, we reconsider the SF's way deriving the g values. By comparing the observed excitation spectra for the Zeeman components with the calculations by Lin-Chung and Wallis[38] and BR,[40] SF have chosen an assignment out of 32 possibilities for the D-line spectra (Fig. 23 in Ref. 33): Their guiding principle was to adopt the values which are close to the theoretical values. We searched whether an alternative assignment was possible by unloosing a little their guiding principle. Then, we found a new reasonable assignment, which explains the C-line as well as D-line spectra and their magnetic field dependences, by exchanging D_4 and D_5 transitions in Fig. 23 of Ref. 33.[36] The new g values of B-doped Ge are given in Table II at the second entry for SF. They are in good agreement with those obtained from the MARA. Moreover, by using the new g values, we can explain the G-line spectra, which is not explained by the SF's assignment[33]: The small splitting of the G line is ascribed to the small g values of the acceptor ground state.[36]

The g values obtained in the present investigation are much less than those calculated in the effective mass theory (Table II). It should be noted, however, that the theoretical g values are sensitive to the values of the valence-band parameters, as pointed out by Suzuki, Okazaki, and Hasegawa.[21] The present formulas for the Zeeman splittings of the acceptor ground state are derived under the following assumptions: The unperturbed ground state is separated from both the excited states and the valence-band edge, and the magnetic field is so small that the splittings of each level can be treated independently. This means that the theory described in Sec. III B is valid when γ is small compared with unity, where γ is the parameter for the magnetic field introduced by Yafet, Keyes, and Adams.[45]

When we calculate the parameter γ for p-Ge, the following results are obtained at 100 kG: $\gamma = 0.3$ when we take the heavy hole mass $0.3m_0$ (m_0 is the free electron mass), whereas $\gamma = 6.7$ when we take the light hole mass $0.04m_0$. Thus, although the MARA are explained successfully, the derived Zeeman-splitting parameters may include some errors since the theory may have been used beyond the limit.

The g values of the acceptor ground state can be derived directly by means of the ESR measurement. In p-Ge, the successful ESR study have not been reported in our knowledge. Mitsuma and Morigaki[46] have searched the ESR signal in p-Ge with X-band microwaves by sweeping the magnetic field from 0 to 15 kG. This means that the ESR signal was searched in the regime $g > 0.48$. The new g values do not conflict with the ESR study.

B. Quadratic Zeeman effect (diamagnetic shift)

The quadratic Zeeman effect is effective for the holes moving in a large orbit under strong magnetic fields as described in Sec. III B. In order to check this, we calculate the coefficient of the quadratic Zeeman effect by taking a simple model. The Hamiltonian of the quadratic Zeeman effect is expressed by

$$H'' = (e^2/2mc^2)\vec{A}^2 \tag{6.1}$$

where the vector potential is given by $\vec{A} = \frac{1}{2}\vec{H} \times \vec{r}$ ($\vec{r}$ is the position vector).

By taking the s-like envelope function of the acceptor ground state as the unperturbed wave func-

tion, the quadratic Zeeman energy (diamagnetic shift) $\Delta E''$ is calculated in the first-order perturbation as

$$\Delta E'' = (e^2 a^{*2}/4mc^2)H^2 \equiv qH^2 . \quad (6.2)$$

The coefficient q is calculated as 0.68×10^{-4} K/kG^2 for p-Ge. This value is of the same order of q_2 and q_3 as shown in Table III.

Now we consider the quadratic Zeeman effect in p-Si and p-GaP by taking the simple model stated above. Using Eq. (6.2), the coefficient q is calculated as 0.11×10^{-4} and 0.08×10^{-4} K/kG^2 for p-Si and p-GaP, respectively. These values are small compared with one for p-Ge.

C. Initial splitting of the acceptor ground state

By comparing the ultrasonic measurement with the theory in the effective mass approximation, it is found that the ground-state quartet of the shallow acceptors in the cubic semiconductors is split due to the internal local fields. The splittings are induced by the static fields which break the tetrahedral symmetry at the acceptor site. In the absence of the external fields, the splitting may be caused by the internal local stresses which are brought about by the randomly distributed crystal imperfections and the dislocations as well as weak correlations among the acceptor impurities.[24,36] We have characterized the feature of these splittings by the Gaussian distribution function in order to make the calculation tractable. Consequently, the average splitting Δ_0 does not vary appreciably with the acceptor concentration in our samples. The value of σ vary slightly. It should be noted, however, that these values of Δ_0 and σ were obtained by the comparison of the MARA line shape under the high magnetic field with the theory as described in Sec. V.

D. Relation to the magnetothermal conductivity measurement

We consider the magnetothermal conductivity in lightly-Ga-doped Ge by Challis *et al.*[29,31] The magnetothermal conductivity in p-Si has been explained by the SM model[27] modified by taking the linear Zeeman effect. However, the conductivity in p-Ge could not be explained by this model. Challis *et al.*[29,31] ascribed the anomalous behavior in p-Ge to the existence of the low-lying excited states by the dynamic Jahn-Teller effect for the acceptor state.[30] The energy spacing between the ground state and the low-lying excited states are smaller for Ga in Ge than for B in Si provided that the values of the deformation-potential constants are similar in these materials.[32] Therefore, if the anomalous behavior in the magnetothermal conductivity in p-Ge is caused by the excited states, a similar anomaly should be observed in p-Si, in contradiction to the experiment.

We consider that the reported anomalous behavior of the magnetothermal conductivity in p-Ge stems from the use of the inadequate Zeeman-splitting parameters and the neglect of the quadratic Zeeman effect. Now we calculate the magnetothermal conductivity in p-Ge at low temperatures by using the new g values and taking account of the quadratic Zeeman effect. We use the usual semiphenomenological expression for the lattice thermal conductivity after SM.[27] In the calculation, we consider the case of $\vec{H} \| [001]$, since the formula becomes too complicated for the case of $\vec{H} \| [110]$, where the conductivity was measured up to 130 kG, and the experimental results show similar behavior for these two cases. We consider first the thermal conductivity assuming that the initial splitting is homogeneous for simplicity. Figure 25 shows the calculated magnetic field dependence of the conductivity at 2.50 K in the sample of Challis and Halbo.[29] The procedure of the calculation is described in Ref. 36. The conductivity is normalized at 30 kG, above which the present theory can be applied rather well. The calculated conductivity with $\Delta = 0.5$ K increases slightly with increasing the magnetic field and then has a maximum at some field. With further increase of the magnetic field, the conductivity decreases. On the other hand, the conductivities with $\Delta = 1.0$ and 1.5 K decrease with increasing the magnetic field.

In the above calculation, we assumed that the splitting is homogeneous. If we take account of the distribution of the splitting, the calculated magnetic field dependence may be agree well with

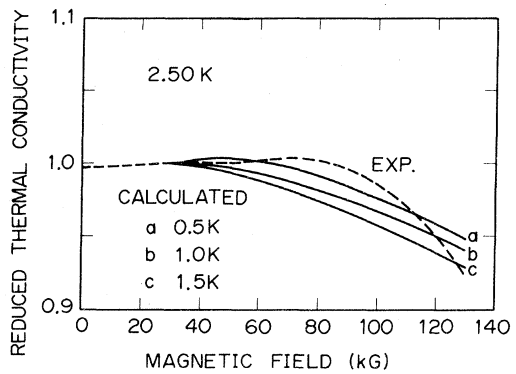

FIG. 25. Calculated magnetic field dependences of the thermal conductivity in p-Ge at 2.50 K under $\vec{H} \| [001]$. Solid lines denoted by a, b, and c indicate the reduced thermal conductivities under uniform splittings $\Delta = 0.5$, 1.0, and 1.5 K, respectively. Broken line indicates the data by Challis *et al.* (Ref. 31) under $\vec{H} \| [110]$.

the experimental one. Further, the adopted splitting is of the order of 1 K, which is much larger than the value obtained from the MARA. This may be ascribed to the fact that, for the study of the thermal conductivity, intimate contact between the thermometer and the sample is required to reduce the contact resistance. So we cannot rule out the possibility of the introduction of the external stress and further the distribution seems to be rather complicated.

Below 30 kG, we cannot make a qualitative discussion on the magnetothermal conductivity as well as the ultrasonic attenuation because of the limit of the present theory. However, we can say that, in low magnetic fields, the movements of each Zeeman sublevels by applying the magnetic field are very slow as shown in Fig. 16 reflecting the small g values. This may explain the fact that the change of the conductivity was slight.

VII. SUMMARY AND CONCLUDING REMARKS

We have shown that the observed MARA, as functions of the acoustic frequency, the temperature, the magnetic field direction, the acceptor concentration, the acoustic power, the acoustic mode, the propagation direction, and the uniaxial stress, are explained consistently in terms of the interaction of the ultrasonic waves with the gallium-acceptor ground state described by the effective mass approximation. Consequently, we could determine the Zeeman-splitting parameters. We have shown that the g values reported by SF cannot explain the MARA, but by reexamining the assignment of SF's data, we have shown that g values which are close to the present results are derived. The present g values seem to be useful to explain the magnetothermal conductivity and consistent with the fact that the ESR signals have not been detected by sweeping the magnetic field in the region corresponding to $g > 0.48$. We have shown that the quadratic Zeeman effect is appreciable in p-Ge, whose effect becomes comparable with the ordinary linear Zeeman effect near 100 kG.

From the analysis of the MARA line shape near 100 kG, we have estimated the initial splitting of the acceptor ground state. By using the estimated splittings, we have calculated the level widths and we have shown that the level width becomes too narrow if we consider that the impurities are isolated. The transverse relaxation via the interaction among the impurities may be an additional mechanism to the level broadening.

Finally, it is worthwhile to point out some limitations of the theory described in Sec. III, which have been noticed during the study. First, the present formulas for the ultrasonic attenuation do not take account of the local equilibrium of the acceptor holes and therefore seem to be valid except for $\omega\tau \ll 1$, where ω is the angular frequency of the phonons and τ is the relaxation time of the acceptor holes. This means that the theory is useful in the low-temperature range, e.g., below 4.2 K.[47] Secondly, the present theory is valid when the Zeeman splittings of the acceptor ground state are larger than the initial splittings due to the internal stresses, i.e.,

$$|E_{14}| \text{ or } |E_{23}| > |\Delta_0| .$$

On the other hand, the present formulas for the Zeeman splittings are valid when γ is small compared with unity as described in Sec. VI A. Thirdly, as causes of the initial splittings, the internal local stresses caused by the crystal imperfections and the interactions among the acceptors are considered. However, there is no tractable way to calculate these with a reasonable precision so that we can compare with the experimental results.

Instead of the present procedure, the existence of the dynamic Jahn-Teller effect for the acceptor state in germanium has been proposed to explain the magnetothermal conductivity.[29] We cannot rule out the possibility of the effect. However, we have explained the MARA and other phenomena in terms of the acceptor-hole-lattice interaction in the effective mass approximation.

ACKNOWLEDGMENTS

We wish to express our sincere thanks to Professor K. Suzuki and Professor N. Mikoshiba for their useful comments and discussions on the present work. It is our pleasure to express appreciation to Professor H. Kawamura for his interest in this work. We are much obliged to Professor L. J. Challis for his comment by which this detailed study was motivated and for communicating their results prior to publication. We are grateful to Dr. K. Kajimura and Dr. R. Inaba for their supports in the course of this work. Thanks are due to S. Morita and K. Mitsugi for the support to supply us with liquid helium.

APPENDIX A

The expressions of $E_{nn'}$, $C_{qt}^{nn'}$, Γ_n^q, and N_n for the transverse waves ($t = 2$) propagating along either the [001] or the [110] direction under $\vec{H} \parallel [001]$ are obtained as follows: From Eqs. (3.10) and (5.5),

$$E_{12} = \Delta_0 + \zeta X + \mu_B(g_1' + \tfrac{13}{4}g_2')H + 2(q_2 + q_3)H^2, \quad \text{(A1)}$$

$$E_{13} = \Delta_0 + \zeta X + \mu_B(2g_1' + \tfrac{7}{2}g_2')H + 2(q_2 + q_3)H^2, \quad \text{(A2)}$$

$$E_{42}=\Delta_0+\zeta X-\mu_B(2g_1'+\tfrac{7}{2}g_2')H+2(q_2+q_3)H^2\,, \quad \text{(A3)}$$

$$E_{43}=\Delta_0+\zeta X-\mu_B(g_1'+\tfrac{13}{4}g_2')H+2(q_2+q_3)H^2\,. \quad \text{(A4)}$$

$C_{\vec{q}t}^{nn'}$ are given by

$$|C_{\vec{q}2}^{nn}|^2=0 \quad \text{for } n=1,2,3,4,$$
$$|C_{\vec{q}2}^{12}|^2=|C_{\vec{q}2}^{34}|^2=0.75, \quad |C_{\vec{q}2}^{13}|^2=|C_{\vec{q}2}^{24}|^2=0\,. \quad \text{(A5)}$$

Γ_n^d can be calculated as

$$\Gamma_1^d=\frac{(D_{u'}^a)^2}{45\pi\rho\hbar^3}\left(E_{12}^3\frac{2}{1-\exp(-E_{12}/kT)}Q(E_{12})+E_{13}^3\frac{D^2+1}{1-\exp(-E_{13}/kT)}Q(E_{13})\right), \quad \text{(A6)}$$

$$\Gamma_2^d=\frac{(D_{u'}^a)^2}{45\pi\rho\hbar^3}\left(E_{21}^3\frac{2}{1-\exp(-E_{21}/kT)}Q(E_{21})+E_{24}^3\frac{D^2+1}{1-\exp(-E_{24}/kT)}Q(E_{24})\right), \quad \text{(A7)}$$

$$\Gamma_3^d=\frac{(D_{u'}^a)^2}{45\pi\rho\hbar^3}\left(E_{31}^3\frac{D^2+1}{1-\exp(-E_{31}/kT)}Q(E_{31})+E_{34}^3\frac{2}{1-\exp(-E_{34}/kT)}Q(E_{34})\right), \quad \text{(A8)}$$

$$\Gamma_3^d=\frac{(D_{u'}^a)^2}{45\pi\rho\hbar^3}\left(E_{42}^3\frac{D^2+1}{1-\exp(-E_{42}/kT)}Q(E_{42})+E_{43}^3\frac{2}{1-\exp(-E_{43}/kT)}Q(E_{43})\right), \quad \text{(A9)}$$

with

$$Q(E)=v_L^{-5}f^2(E/\hbar v_L)+\tfrac{3}{2}v_T^{-5}f^2(E/\hbar v_T)\,, \quad \text{(A10)}$$

$$f(q)=(1+a^{*2}q^2/4)^{-2}\,, \quad \text{(A11)}$$

where v_L and v_T are the average velocities of the longitudinal and transverse waves in the elastically isotropic media. N_n is expressed by

$$N_n=N\left[\sum_{i=1}^{4}\exp\left(\frac{-E_{ni}}{kT}\right)\right]\,, \quad \text{(A12)}$$

where N is the acceptor concentration per unit volume.

In using the theory described in Sec. III, the following facts should be taken into account: (i) In order to make the calculated attenuation to be comparable with the observed one, we use a scaling factor β,[19,24] which is usually less than unity. (ii) The attenuation coefficient consists of the resonance and the relaxation terms.[19,36] (iii) The formulas in the presence of the magnetic field are useful under strong magnetic fields, e.g., above 30 kG in the present case, where the Zeeman splittings of the acceptor ground state are larger than the initial splittings as shown in Fig. 18.

APPENDIX B

The left-hand side of the resonance conditions, (5.1) and (5.2), are rewritten by the following parabola:

$$f_\pm(X,H)=2(q_2+q_3)(H-H_0)^2+\Delta_0+\zeta X-2(q_2+q_3)H_0^2\,, \quad \text{(B1)}$$

where

$$H_0=\mp\mu_B(g_1'+\tfrac{13}{4}g_2')/4(q_2+q_3)\,. \quad \text{(B2)}$$

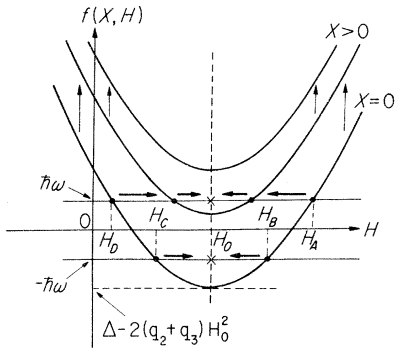

FIG. 26. Schematic representation of the function $f(\vec{X},\vec{H})$. The vertical arrows indicate the increasing direction of $\vec{X}$, and the corresponding shifts of the resonance fields denoted by H_A, H_B, H_C, and H_D are indicated by the horizontal arrows.

When double signs appear in the expressions, the upper and the lower signs correspond to conditions (5.1) and (5.2), respectively. Each parabola of $f_\pm(X,H)$ is classified into four cases according to the coefficients as (5.6). We find that the parabolas $f_+(X,H)$ for the cases (a), (b), (c), and (d) in (5.6) have the same properties as the parabolas $f_-(X,H)$ for the cases (b), (a), (d), and (c), respectively.

First, we consider the case (b) for $f_+(X,H)$ and the case (a) for $f_-(X,H)$ (Fig. 26). When $\Delta_0-2(q_2+q_3)H_0^2<-\hbar\omega$ is satisfied at $X=0$, $|f_\pm(X,H)|=\hbar\omega$ gives four roots H_A, H_B, H_C, and H_D as shown in Fig. 26, where the resonance condition is satisfied. When the uniaxial stress is applied, the parabola is raised. Then H_A, H_B, H_C, and H_D shift as shown in Fig. 26. With further increase of X, the roots become two (H_A and H_D) and, when $X>[2(q_2+q_3)H_0^2-\Delta_0]/\zeta$, no roots are found.

Next, we consider the case (a) for $f_+(X,H)$ and the case (b) for $f_-(X,H)$. When we calculate H_0 according to Eq. (B2), we find that H_0 has a negative value for these two cases. Lastly, we consider the remaining cases. Since (q_2+q_3) is negative, the resonance fields shift in opposite directions to ones shown in Fig. 26.

Now let us compare the observed resonance-peak positions under $\vec{H}\|[001]$ and $\vec{X}\|[001]$ shown in Fig. 15 with the above resonance condition. The observed resonance-peak positions of the peaks

A and B were shifted toward lower magnetic fields with increasing the uniaxial stress. On the other hand, the resonance-peak positions of the peaks C and D were shifted toward higher magnetic fields with increasing the uniaxial stress. These peaks disappeared at $H_0 = 45$ kG. These features are explained if we regard the resonance fields of the peaks A, B, C, and D as H_A, H_B, H_C, and H_D, respectively, in the case (b) for $f_+(X,H)$ and the case (a) for $f_-(X,H)$.

[1]R. W. Keyes, Phys. Rev. 122, 1171 (1961).
[2]A. Griffin and P. Carruthers, Phys. Rev. 131, 1976 (1963).
[3]J. F. Goff and N. Pearlman, Phys. Rev. 140, A2151 (1965); M. P. Mathur and N. Pearlman, *ibid* 180, 833 (1969).
[4]K. Suzuki and N. Mikoshiba, J. Phys. Soc. Jpn. 31, 186 (1971).
[5]J. A. Carruthers, T. H. Geballe, H. M. Rosenberg, and J. M. Ziman, Proc. Roy. Soc. Lond. A 238, 502 (1957); J. A. Carruthers, J. F. Cochran, and K. Mendelssohn, Cryogenics 2, 168 (1962).
[6]L. J. Challis, J. D. N. Cheeke, and J. B. Harness, Philos. Mag. 7, 1941 (1962).
[7]A. M. Poujade and H. J. Albany, Phys. Rev. 182, 802 (1969).
[8]J. C. Thompson and B. A. Younglove, J. Phys. Chem. Solids 20, 146 (1961).
[9]M. G. Holland, in *Semiconductors and Semimetals*, edited by R. K. Willardson and A. C. Beer (Academic, New York, 1966), Vol. 2, p. 3.
[10]K. Suzuki and N. Mikoshiba, in *Proceedings of the International Conference on Phonon Scattering in Solids, Paris, 1972* (Commissariat a l'Energie Atomique, Service de Documentation, Saclay, 1972), p. 125.
[11](a) R. W. Keyes, IBM J. Res. Dev. 5, 266 (1961); (b) in *Solid State Physics*, edited by F. Seitz and D. Turnbull (Academic, New York, 1967), Vol. 20, p. 37.
[12]M. Pomerantz, Proc. IEEE 53, 1438 (1965); Phys. Rev. B 1, 4029 (1970).
[13]K. Suzuki and N. Mikoshiba, Phys. Lett. 23, 44 (1966); J. Phys. Soc. Jpn. 28, 1248 (1970).
[14]P. C. Kwok, Phys. Rev. 149, 666 (1966).
[15]T. Ishiguro and N. Mikoshiba, J. Phys. Chem. Solids 31, 1729 (1970).
[16]T. Miyasato, F. Akao, and M. Ishiguro, J. Phys. Soc. Jpn. 35, 1668 (1973).
[17]W. P. Mason and T. Bateman, Phys. Rev. 134, A1386 (1964).
[18]M. Pomerantz, in Proceedings of the Symposium on Acoustoelectronics, Sendai, 1968 (unpublished), p. 39.
[19]K. Suzuki and N. Mikoshiba, Phys. Rev. Lett. 28, 94 (1972). It should be noted that, for the fast transverse waves propagating along the [110] direction, $\alpha_1(\Delta)$ and $\alpha_2(\Delta)$ in this reference, should be multiplied by factors 4 and 2, respectively.
[20]H. Hasegawa, Phys. Rev. 129, 1029 (1963).
[21]K. Suzuki, M. Okazaki, and H. Hasegawa, J. Phys. Soc. Jpn. 19, 930 (1964).
[22]W. Kohn, in Ref. 11(b), Vol. 5, p. 257.
[23]T. Ishiguro and H. Tokumoto, J. Phys. Soc. Jpn. 37, 1716 (1974).
[24]T. Ishiguro, Phys. Rev. B 8, 629 (1973).
[25]T. Ishiguro, T. A. Fjeldly, and C. Elbaum, Solid State Commun. 10, 1039 (1972).
[26]T. Ishiguro, K. Suzuki, and N. Mikoshiba, in *Proceedings of the International Conference on the Physics of Semiconductors, Warsaw, 1972* (Polish Scientific, Warsaw, 1972), p. 1239.
[27]K. Suzuki and N. Mikoshiba, Phys. Rev. B 3, 2550 (1971); J. Phys. Soc. Jpn. 31, 44 (1971).
[28]T. Fjeldly, T. Ishiguro, and C. Elbaum, Phys. Rev. B 7, 1932 (1973).
[29]L. J. Challis and L. Halbo, Phys. Rev. Lett. 28, 816 (1972); L. Halbo and L. J. Challis, in Ref. 10, p. 139.
[30]T. N. Morgan, Phys. Rev. Lett. 24, 887 (1970).
[31]L. J. Challis, S. C. Haseler, M. W. S. Parsons, and J. Rivallin, in *Phonon Scattering in Solids*, edited by L. J. Challis, V. W. Rampton, and A. F. G. Wyatt (Plenum, New York and London, 1976), p. 328.
[32]H. Tokumoto, T. Ishiguro, R. Inaba, K. Kajimura, K. Suzuki, and N. Mikoshiba, Phys. Rev. Lett. 32, 717 (1974).
[33]H. P. Soepangkat and P. Fisher, Phys. Rev. B 8, 870 (1973).
[34]F. H. Pollak, Phys. Rev. 138, A168 (1965).
[35]L. M. Roth, Phys. Rev. 118, 67 (1960).
[36]H. Tokumoto, Researches of the Electrotechnical Laboratory No. 768 (1977) (unpublished).
[37]G. L. Bir, E. I. Butikov, and G. E. Pikus, J. Phys. Chem. Solids 24, 1467 (1963).
[38]P. J. Lin-Chung and R. F. Wallis, J. Phys. Chem. Solids 30, 1453 (1969).
[39]W. Kohn and D. Schechter, Phys. Rev. 99, 1903 (1955); D. Schechter, J. Phys. Chem. Solids 23, 237 (1962); K. S. Mendelson and H. M. James, *ibid* 25, 729 (1964).
[40]A. K. Bhattacharjee and S. Rodriguez, Phys. Rev. B 6, 3836 (1972).
[41]E. Ortlieb, Hp. Schad, and K. Lassmann, in Ref. 31, p. 334.
[42]J. C. Hensel and K. Suzuki, Phys. Rev. B 9, 4219 (1974).
[43]C. P. Slichter, *Principles of Magnetic Resonance* (Harper and Row, New York, 1963), p. 4.
[44]J. Joffrin and A. Levelut, J. Phys. (Paris) 36, 811 (1975).
[45]Y. Yafet, R. W. Keyes, and E. N. Adams, J. Phys. Chem. Solids 1, 137 (1956).
[46]T. Mitsuma and K. Morigaki (unpublished; we thank Professor K. Morigaki for helpful conversations).
[47]K. Suzuki (private communication).